Digital Signal Processing 137 (2023) 104048

Contents lists available at ScienceDirect

Digital Signal Processing

journal homepage: www.elsevier.com/locate/dsp

A general framework for hepatic iron overload quantification using MRI

Ahmed Karam Eldaly [a,b,*], Ayman M. Khalifa [b]

[a] Centre for Medical Image Computing, Department of Computer Science, University College London, London, United Kingdom
[b] Biomedical Engineering Department, Faculty of Engineering, Helwan University, Cairo, Egypt

ARTICLE INFO

Article history:
Available online 14 April 2023

Keywords:
MRI
Liver
Iron overload
T2*
Thalassemia
ADMM

ABSTRACT

Magnetic resonance imaging (MRI) has been considered for the quantification of iron overload in the liver. Iron overload was found to correlate with T2* measurement using T2* weighted images. In this work, we address the problem of iron overload estimation in the liver using MRI. We propose a general framework for all liver models proposed in the literature. The iron overload estimation task is then formulated as a minimization problem, and suitable regularization functions are assigned to the unknown model parameters. Subsequently, an alternating direction method of multipliers (ADMM) is used to estimate these unknown parameters. Three different models are derived, tested and compared; namely the single exponential (SEXP), the bi-exponential (BiEXP), and the exponential plus constant (CEXP). Simulations conducted using synthetic datasets indicate good correlation between estimated and ground truth T2* for all models. Moreover, the algorithms are evaluated using MRI scans of nine patients of different iron concentrations, using a 3-Tesla MRI scanner. The estimated T2* values of the proposed approaches are found to correlate with those obtained by the MRI scanner console. Moreover, the proposed approaches outperform several existing methods in the literature for iron overload estimation.

1. Introduction

1.1. Thalassemias

Thalassemias are genetic disorders causing the body to produce insufficient hemoglobin and red blood cells. The repeated transfusions by chronic blood transfusion cause progressive accumulation of iron in different body organs. Thalassemia major patients receive around 0.4 mg/kg/day of heme iron, that is 10 to 50 times the physiologic rate of iron absorption [41]. This iron overload by this transfusion mainly increases due to intestinal iron absorption by tissue hypoxia, apoptosis of defective erythroid precursors generated by ineffective erythropoiesis, and hemolysis of native and transfused red blood cells [31]. Due to the additive iron-loading operations, iron overload becomes severe in early childhood. Patients must undergo iron chelation therapy, otherwise affected patients die from endocrine and cardiac dysfunction in the second decade of life [4,8,18].

1.2. Iron overload

Hepatic iron overload may cause poor life quality and even lead to mortality. Hence, liver iron quantification is important for such patients. In hereditary hemochromatosis (HH), quantification of iron overload in the liver enables identification of patients suitable for phlebotomy therapy and helps exclude clinical disease in patients at risk for HH based on genetic studies. Quantification of liver iron content also gives important foreknowledge regarding the risk for developing hepatic complications such as hepatic fibrosis and cirrhosis [7,1]. On the other hand, in thalassemias and other iron-loading anemias, quantification of liver iron content provides an indication of the total body iron content [5]. Around 70% of total body iron is deposited in the liver and hence is the main iron storage site [13]. Therefore, it was found that the iron content in the liver correlates closely with total body iron and accounts. Thus, quantifying liver iron content is an indicative of total body iron to guide, monitor, and initiate therapy [13]. Hepatic iron content also serves as a biomarker for endocrine and cardiovascular complications in patients with thalassemias. Usually mild iron overload can be an assisting factor in the development of hepatic disorders [20], hence quantifying the iron content in the liver is now considered relevant in the management of chronic liver diseases such as viral hepatitis, alcoholic liver disease, non-alcoholic

* Corresponding author at: Centre for Medical Image Computing, Department of Computer Science, University College London, London, United Kingdom.
E-mail addresses: a.karam@ucl.ac.uk (A. Karam Eldaly), A.Khalifa@h-eng.helwan.edu.eg (A.M. Khalifa).

https://doi.org/10.1016/j.dsp.2023.104048

fatty liver disease, and porphyria cutanea tarda [33]. Liver biopsy is currently the gold standard technique for quantifying iron content in the liver. However, due to the technique's invasiveness, high cost, and the sampling error, it limits its widespread use. On the other hand, serum ferritin could be used for quantifying iron content. However, this technique can be affected by inflammation and infection, and hence becomes nonspecific [28].

1.3. MRI for iron overload estimation

Recently, magnetic resonance imaging (MRI) has been considered for evaluating iron content using T2* measurement [9,3,34,40], and has shown promising results. By plotting the signal intensity of a number of T2*-weighted images at different time to echo (TE's), against TE, the T2* (measured in ms), and its inverse $r = 1/\text{T2}^*$ (measured in $1/s$), can be calculated using curve fitting. It has been shown that iron content in the liver results in abnormally reduced T2* values that were not observed in other clinical conditions.

In the literature, there has been several approaches for estimating T2* values in T2*-weighted sequence of the liver. All these methods consider fitting the signal intensities acquired at multiple TE's to an exponentially decaying curve using the Levenberg Marquardt algorithm [34,38,35,27,26,24,23,25,13]. Although the analysis process is conceptually straightforward, there are a number of factors that could affect the resulting T2* value, including the choice of the fitting model, way of processing the intensities (voxel-wise, average/median of a number of voxels, etc.) and region of interest (ROI). Due to the heterogeneous iron concentration in the liver, susceptibility artifacts, and inclusion of vasculature, the user's selection of the ROI for estimation of T2* affects the results, which results in partial volume effect that affects T2* measurement of the liver parenchyma [38]. T2* can be calculated pixel-wise (relaxivity map). However, due to these reasons, T2* computation inside a defined ROI is preferred to avoid heterogeneous results between adjacent pixels. On the other hand, the choice of the appropriate exponential fitting model is critical for T2* calculation. There has been several models proposed in the literature, including the single-exponential, the bi-exponential and the exponential plus constant models [39,35,34,32].

1.4. Model for data fitting

The simplest model for data fitting is a single-exponential model given by,

$$\mathbf{s} = a \exp\left(-r\mathbf{t}\right), \tag{1}$$

where $\mathbf{s}$ is measured signal intensity, a is the signal intensity expected at TE $= 0$, r is the reciprocal of T2*, e.g. $r = 1/\text{T2}^*$, and $\mathbf{t} =$ TE is time to echo vector. The limitation of this model is that it assumes uniform iron concentration within each tissue voxel, which was found to be incorrect [17], as the voxels may contain both iron-dense (iron-loaded hepatocytes and/or Kupffer cells) and iron-sparse components (bile, blood, interstitial fluid) [42]. These components act in an opposite manner, that the iron-dense one generates rapidly decaying signal, whereas the iron-sparse one generates slowly decaying signal. Hence, following this, the single-exponential fitting model assumes, as a simplification, that a single exponential describes the contributions of both components.

Numerous data-fitting models have been proposed to address the limitations of the single-exponential model mentioned above [8,10,34,29,17,22,16], including

1. The single-exponential model with offset (CEXP). In this model, a constant offset c is added to account for long T2* components. This model can be written as,

$$\mathbf{s} = a \exp\left(-r\mathbf{t}\right) + c. \tag{2}$$

2. The bi-exponential model (BiEXP). In this model, two components are considered in the modelling process: an iron-dense, short-T2* component and an iron-sparse, long-T2* component). This model can be written as,

$$\mathbf{s} = a \exp\left(-r_1\mathbf{t}\right) + b \exp\left(-r_2\mathbf{t}\right), \tag{3}$$

where a and b are the iron-dense, short-T2* and iron-sparse, long-T2* components, respectively, and r_1 and r_2 are their corresponding inverse T2*.

Each of the two models mentioned above has pros and cons, and consensus has not yet been reached regarding which model is optimal for T2* estimation.

1.5. Contributions

In this work, we address the problem of iron content estimation in thalassemia patients using magnetic resonance imaging. The main contributions of this work are fourfold.

1. We propose a general framework for the problem of iron overload estimation in the liver using MRI. To the best of our knowledge, it is the first time in the literature this general framework is introduced.
2. We formulate the iron overload estimation task as an optimization problem, assign suitable regularization functions to the unknown model parameters and use an alternating direction method of multiplier to estimate these parameters. To the best of our knowledge this is the first time in the literature this problem is formulated and solved using such way.
3. We test and compare three different types of imaging models, namely the single exponential (SEXP), the bi-exponential (BiEXP) and the exponential plus constant (CEXP), using extensive simulations conducted using synthetic datasets where ground truth is available, and using real patient datasets of different iron overload. The proposed methods are compared against several existing methods in the literature.
4. We develop algorithms dedicated to images that follow the exponential decaying models, which do not rely on strong assumptions about the modality or the application. The developed methods can thus be applied to a wide range of imaging systems and applications, including myocardial iron overload estimation, life-time estimation in fluorescence microscopy, and others.

The remaining sections of the paper are organized as follows. Section 2 provides a general formulation to the problem of iron overload estimation in the liver, followed by Section 3 which summarizes the proposed model and an ADMM estimation strategy to recover the unknown model parameters. Section 4 provides the derivation of three different algorithms; namely SEXP, BiEXP, and CEXP, from the general framework proposed in Section 3. Simulations conducted using synthetic, and real patient datasets are presented in Sections 5 and 6, respectively. Limitations, conclusions and suggestions for future work are finally reported in Sections 7 and 8 respectively.

2. Problem formulation

Fig. 1 shows an example of two decay curves of different T2* values akin to those obtained using T2* weighted images. As the

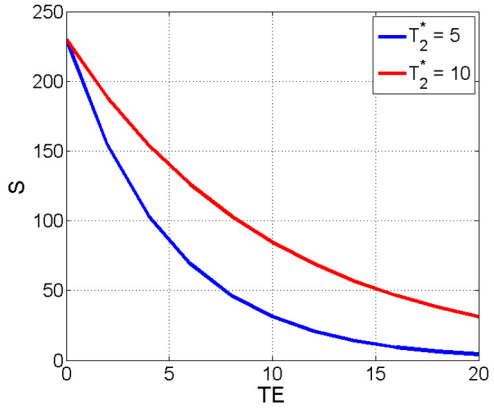

Fig. 1. Plot of time to echo (TE) versus corresponding intensity values, for $T2^* = 5$ and $T2^* = 10$.

time to echo (TE) increases, the intensity follows an exponential decaying model with a time constant T2*. The higher the iron concentration is, the faster the decay of the intensities when TE increases, and hence the lower the corresponding T2* value. The core idea is to estimate the time constant T2*, which is an indicative to the total iron content in the liver. However, with the presence of noise and vasculature, the estimation of the T2* value, and hence the iron concentration, becomes difficult. In this work, we propose a robust, yet fast general framework for T2*estimation using T2* weighted magnetic resonance images.

For simplicity, in the rest of the manuscript, we denote TE vector by $\mathbf{t} = [t_1, t_2, \cdots, t_M] \in \mathbb{R}^M$ and $r = \frac{1}{T2^*}$. Hence, given a sequence of magnetic resonance images (each of size $K \times L$) of the liver taken at different TE, denoted by $\mathbf{S} \in \mathbb{R}^{K\times L\times M}$, for signal intensities of voxel n, denoted as $\mathbf{s}_n = [s_1, s_2, \cdots, s_M] \in \mathbb{R}^M$, the problem of r estimation of voxel n is formulated such that

$$\mathbf{s}_n = \sum_{i=1}^{I} a_{n_{(i)}} \exp\left(-r_{n_{(i)}}\mathbf{t}\right) + c_n + \mathbf{w}_n, \tag{4}$$

where $a_n = \{a_{n_{(1)}}, a_{n_{(2)}}, \cdots, a_{n_{(I)}}\}$ are set of scalars representing physical phenomena, including initial signal intensity when $\mathrm{TE} = 0$, iron-dense and iron-sparse, components, etc., c_n is an offset which may account for long T2* components, and $\mathbf{w}_n$ is a low-energy noise component, which is assumed to be independent and identically distributed (i.i.d.) Gaussian with zero mean [6,21]. Setting c_n to $c_n = 0$ and $I = 1$, in Eq. (4) give the single exponential model as follows

$$\mathbf{s}_n = a_n \exp\left(-r_n\mathbf{t}\right) + \mathbf{w}_n, \tag{5}$$

whereas, setting c_n to $c_n = 0$ and $I = 2$ give the bi-exponential model, given by

$$\mathbf{s}_n = \sum_{i=1}^{2} a_{n_{(i)}} \exp\left(-r_{n_{(i)}}\mathbf{t}\right) + \mathbf{w}_n, \tag{6}$$

and finally setting I to $I = 1$ gives the exponential plus constant model, which can be written as

$$\mathbf{s}_n = a_n \exp\left(-r_n\mathbf{t}\right) + c_n + \mathbf{w}_n. \tag{7}$$

The primary objective here is that, for each voxel, we need to estimate the $\mathbf{r}$ constant(s) using the model mentioned above in Eq. (4), from the observations $\mathbf{s}$. However, the signal intensities $\mathbf{a} = \{\mathbf{a}_{(1)}, \mathbf{a}_{(2)}, \cdots, \mathbf{a}_{(I)}\}$ and the offset $\mathbf{c}$ are also unknown. Thus we propose to estimate jointly $(\mathbf{r}, \mathbf{a}, \mathbf{c})$ from the observations $\mathbf{s}$. To solve this problem, we propose an optimization-based method to estimate the unknown parameters.

3. Proposed model

The recovery of $\mathbf{a}$, $\mathbf{r}$ and $\mathbf{c}$ using the general model in Eq. (4) is formulated as the following unconstrained minimization problems

$$\begin{aligned}\underset{\{\mathbf{a}_{(i)},\mathbf{r}_{(i)}\}_{i=1}^{I},\mathbf{c}}{\text{minimize}} \; & \sum_{n=1}^{N=K\times L} \frac{1}{2}\|\mathbf{s}_n - \sum_{i=1}^{I} a_{n_{(i)}} \exp\left(-r_{n_{(i)}}\mathbf{t}\right) - c_n\|_2^2 \\ & + \sum_{i=1}^{I} \left(\alpha_{(i)}\Phi_1(\mathbf{a}_{(i)}) + \beta_{(i)}\Phi_2(\mathbf{r}_{(i)})\right) + \gamma\Phi_3(\mathbf{c}),\end{aligned} \tag{8}$$

where $\Phi_1(\mathbf{a})$, $\Phi_2(\mathbf{r})$ and $\Phi_3(\mathbf{c})$ are regularization functions on $\mathbf{a}$, $\mathbf{r}$ and $\mathbf{c}$ respectively, α, β and γ are positive scalar parameters controlling the degree of regularization of $\mathbf{a}$, $\mathbf{r}$ and $\mathbf{c}$ respectively, and $\|\cdot\|_2$ denotes the ℓ_2-norm. In this work, we promote spatial correlation between voxels, thus the variables $\mathbf{a}$ and $\mathbf{r}$ are assigned total variation (TV) regularization e.g., $\Phi_1(\mathbf{a}) = \|\mathbf{a}\|_{\mathrm{TV}}$ and $\Phi_2(\mathbf{r}) = \|\mathbf{r}\|_{\mathrm{TV}}$. The TV of observed signals with excessive detail tend to be high, that is the integral of the absolute image gradient is high. According to this principle, minimizing the TV of the signal — subject to data fidelity — suppresses unwanted detail whilst preserving important details such as edges [36]. On the other hand, in order to preserve the conjugacy of the parameter $\mathbf{c}$, we assume that it is smooth, and hence it is assigned $\Phi_3(\mathbf{c}) = \|\mathbf{c}\|_2^2$. Therefore, problem (8) can be written as follows

$$\begin{aligned}\underset{\{\mathbf{a}_{(i)},\mathbf{r}_{(i)}\}_{i=1}^{I},\mathbf{c}}{\text{minimize}} \; & \sum_{n=1}^{N=K\times L} \frac{1}{2}\|\mathbf{s}_n - \sum_{i=1}^{I} a_{n_{(i)}} \exp\left(-r_{n_{(i)}}\mathbf{t}\right) - c_n\|_2^2 \\ & + \sum_{i=1}^{I} \left(\alpha_{(i)}\|\mathbf{a}_{(i)}\|_{\mathrm{TV}} + \beta_{(i)}\|\mathbf{r}_{(i)}\|_{\mathrm{TV}}\right) + \gamma\|\mathbf{c}\|_2^2.\end{aligned} \tag{9}$$

The TV function can be written as follows. For a given vectorization $\mathbf{x} \in \mathbb{R}^N$ of an image $\mathbf{X} \in \mathbb{R}^{K\times L}$, the anisotropic 2D TV semi-norm is defined as [36,14]

$$\|\mathbf{x}\|_{\mathrm{TV}} = \sum_{n=1}^{N=K\times L} |\Delta_n^h\mathbf{x}| + |\Delta_n^v\mathbf{x}| = \|\mathbf{D}\mathbf{x}\|_1, \tag{10}$$

where $\Delta_n^h\mathbf{x}$ and $\Delta_n^v\mathbf{x}$ denote the vertical and horizontal first order differences at pixel n, $\|\cdot\|_1$ is the ℓ_1-norm (sum of absolute values), and the matrix $\mathbf{D} \in \mathbb{R}^{2N\times N}$ is the vertical concatenation of both the horizontal and vertical first order differences. This regularizer is a discrete version of the TV regularizer proposed in [36]. The optimization problem in equation (9) (and also Eq. (8)), although convex, cannot be solved using standard gradient-based methods due to the non-smooth terms. The core idea is to convert this unconstrained minimization problem into another constrained one by the application of a variable splitting operation (see Eq. (11) below). Finally, the obtained constrained problems are solved with using the alternating direction method of multipliers (ADMM) [2,30,19]. By a careful choice of the new variables, the initial problems are converted into a sequence of much simpler problems, which can be solved iteratively.

To solve the problems depicted in Equation (9), we introduce new variables $\mathbf{y}$ and $\mathbf{z}$ for the regularization functions Φ_1 and Φ_2 respectively, in order to decouple them from the data fidelity term. Therefore, the constrained version of problem Eq. (9) can be written as follows

$$\underset{\{\mathbf{a}_{(i)},\mathbf{r}_{(i)},\mathbf{y}_{(i)},\mathbf{z}_{(i)}\}_{i=1}^{I},\mathbf{c}}{\text{minimize}} \sum_{n=1}^{N=K\times L} \frac{1}{2}\|\mathbf{s}_n - \sum_{i=1}^{I} a_{n_{(i)}} \exp\left(-r_{n_{(i)}}\mathbf{t}\right) - c_n\|_2^2 + \sum_{i=1}^{I}\left(\alpha_{(i)}\|\mathbf{y}_{(i)}\|_{\text{TV}} + \beta_{(i)}\|\mathbf{z}_{(i)}\|_{\text{TV}}\right) + \gamma\|\mathbf{c}\|_2^2,$$
$$\text{subject to } \mathbf{y}_{(i)} = \mathbf{a}_{(i)}, \mathbf{z}_{(i)} = \mathbf{r}_{(i)}, \text{ for } i = 1, 2, \cdots, I. \tag{11}$$

Subsequently, the corresponding augmented Lagrangian can be written as

$$\mathcal{L}(\{\mathbf{a}_{(i)}, \mathbf{r}_{(i)}, \mathbf{y}_{(i)}, \mathbf{z}_{(i)}, \mathbf{h}_{(i)}, \mathbf{g}_{(i)}\}_{i=1}^{I}, \mathbf{c}) =$$
$$\sum_{n=1}^{N=K\times L} \frac{1}{2}\|\mathbf{s}_n - \sum_{i=1}^{I} a_{n_{(i)}} \exp\left(-r_{n_{(i)}}\mathbf{t}\right) - c_n\|_2^2 + \sum_{i=1}^{I}\left(\alpha_{(i)}\|\mathbf{y}_{(i)}\|_{\text{TV}} + \beta_{(i)}\|\mathbf{z}_{(i)}\|_{\text{TV}}\right) + \gamma\|\mathbf{c}\|_2^2 + \sum_{i=1}^{I}\frac{\mu}{2}\|\mathbf{y}_{(i)} - \mathbf{a}_{(i)} - \mathbf{h}_{(i)}\|_2^2 + \frac{\mu}{2}\|\mathbf{z}_{(i)} - \mathbf{r}_{(i)} - \mathbf{g}_{(i)}\|_2^2, \tag{12}$$

where $\mathbf{h}$ and $\mathbf{g}$ are the set of Lagrange multipliers corresponding to the splitting, and $\mu > 0$ is a constant. The ADMM algorithm using to solve Eq. (12) is shown in Algorithm 1. During each step of this iterative scheme, $\mathcal{L}$ is optimized with respect to $\mathbf{a}$ (step 4), $\mathbf{r}$ (step 5), $\mathbf{y}$ (step 6), $\mathbf{z}$ (step 7) and $\mathbf{c}$ (step 9); and then the Lagrange multipliers are updated (steps 11 and 12).

Algorithm 1 Iron overload estimation using ADMM.

1: set $k = 0$, choose $\mathbf{a}^{(0)}, \mathbf{r}^{(0)}, \mathbf{c}^{(0)}\mathbf{y}^{(0)}, \mathbf{z}^{(0)}, \mathbf{h}^{(0)}, \mathbf{g}^{(0)}$, and $\mu > 0$
2: **repeat** $(k \leftarrow k + 1)$
3: **For** $i = 1 : I$;
4: $\mathbf{a}_{(i)}^{(k+1)} \leftarrow \min_{\mathbf{a}} \mathcal{L}(\mathbf{a}_{(i)}, \mathbf{r}_{(i)}^{(k)}, \mathbf{c}^{(k)}, \mathbf{y}_{(i)}^{(k)}, \mathbf{z}_{(i)}^{(k)}, \mathbf{h}_{(i)}^{(k)}, \mathbf{g}_{(i)}^{(k)})$,
5: $\mathbf{r}_{(i)}^{(k+1)} \leftarrow \min_{\mathbf{r}} \mathcal{L}(\mathbf{a}_{(i)}^{(k+1)}, \mathbf{r}_{(i)}, \mathbf{c}_{(i)}^{(k)}, \mathbf{y}_{(i)}^{(k)}, \mathbf{z}_{(i)}^{(k)}, \mathbf{h}_{(i)}^{(k)}, \mathbf{g}_{(i)}^{(k)})$,
6: $\mathbf{y}_{(i)}^{(k+1)} \leftarrow \min_{\mathbf{y}} \mathcal{L}(\mathbf{a}^{(k+1)}, \mathbf{r}^{(k+1)}, \mathbf{c}^{(k)}, \mathbf{y}, \mathbf{z}^{(k)}, \mathbf{h}^{(k)}, \mathbf{g}^{(k)})$,
7: $\mathbf{z}_{(i)}^{(k+1)} \leftarrow \min_{\mathbf{z}} \mathcal{L}(\mathbf{a}^{(k+1)}, \mathbf{r}^{(k+1)}, \mathbf{c}^{(k)}, \mathbf{y}^{(k+1)}, \mathbf{z}, \mathbf{h}^{(k)}, \mathbf{g}^{(k)})$,
8: **End**
9: $\mathbf{c}^{(k+1)} \leftarrow \min_{\mathbf{c}} \mathcal{L}(\mathbf{a}_{(i)}^{(k+1)}, \mathbf{r}_{(i)}^{(k+1)}, \mathbf{c}, \mathbf{y}_{(i)}^{(k+1)}, \mathbf{z}_{(i)}^{(k+1)}, \mathbf{h}_{(i)}^{(k)}, \mathbf{g}_{(i)}^{(k)})$,
10: **For** $i = 1 : I$;
11: **Update** $\mathbf{h}_{(i)} : \mathbf{h}_{(i)}^{(k+1)} \leftarrow \mathbf{h}_{(i)}^{(k)} - \left(\mathbf{y}_{(i)}^{(k+1)} - \mathbf{a}_{(i)}^{(k+1)}\right)$,
12: **Update** $\mathbf{g}_{(i)} : \mathbf{g}_{(i)}^{(k+1)} \leftarrow \mathbf{g}_{(i)}^{(k)} - \left(\mathbf{z}_{(i)}^{(k+1)} - \mathbf{r}_{(i)}^{(k+1)}\right)$,
13: **End**
14: **until** some stopping criterion is satisfied.

We now detail each step of Algorithm 1 as follows.

3.1. Solving for $\mathbf{a}$

Given that we run an optimization over the variable $\mathbf{a}$, the terms of the objective function (12) which do not contain this variable are not taken into account. Thus, the reduced optimization function becomes, then

$$\underset{a_{n_{(1)}},\cdots,a_{n_{(I)}}}{\text{minimize}} \sum_{n=1}^{N} \frac{1}{2}\|\mathbf{s}_n - \sum_{i=1}^{I} a_{n_{(i)}} \exp\left(-r_{n_{(i)}}\mathbf{t}\right) - c_n\|_2^2 + \sum_{i=1}^{I}\frac{\mu}{2}\left(y_{n_{(i)}} - a_{n_{(i)}} - h_{n_{(i)}}\right)^2, \tag{13}$$

whose solution is given by

$$a_{n_{(i)}}^{(k+1)} \leftarrow \left(\tilde{\mathbf{u}}_{n_{(i)}}^{(k)} + \mu\right)^{-1}\left((\mathbf{s}_n - c_n^{(k)})\mathbf{u}_{n_{(i)}}^{T^{(k)}} + \mu(y_n^{(k)} + h_{n_{(i)}}^{(k)})\right), \text{ for } i = 1, 2, \cdots, I, \tag{14}$$

with $\mathbf{u}_{n_{(i)}}^{(k)} = \exp\left(-r_{n_{(i)}}^{(k)}\mathbf{t}\right)$, and $\tilde{\mathbf{u}}_{n_{(i)}}^{(k)} = \mathbf{u}_{n_{(i)}}^{(k)^T}\mathbf{u}_{n_{(i)}}^{(k)}$.

3.2. Solving for $\mathbf{r}$

It can be seen from Eq. (12) that solving for the variable $\mathbf{r}$ reduces to solving the following minimization problem

$$\mathbf{r}_{(1)}^*, \cdots, \mathbf{r}_{(I)}^* = \underset{\mathbf{r}_{(1)},\cdots,\mathbf{r}_{(I)}}{\text{minimize}} \quad \mathcal{H}(\mathbf{r}_{(1)}, \cdots, \mathbf{r}_{(I)}), \tag{15}$$

where

$$\mathcal{H}(\mathbf{r}_{(1)}, \cdots, \mathbf{r}_{(I)}) = \sum_{n=1}^{N} \frac{1}{2}\|\mathbf{s}_n - \sum_{i=1}^{I} a_{n_{(i)}} \exp\left(-r_{n_{(i)}}\mathbf{t}\right) - c_n\|_2^2 + \sum_{i=1}^{I}\frac{\mu}{2}\left(z_{n_{(i)}} - r_{n_{(i)}} - g_{n_{(i)}}\right)^2. \tag{16}$$

Since there is no closed form solution to this minimization problem, the solution can be efficiently computed using gradient descent [15]. The update equation for this iterative method is

$$r_{n_{(i)}}^{(p+1)} = r_{n_{(i)}}^{(p)} - \delta\frac{\partial\mathcal{H}(r_{n_{(i)}}^{(p)})}{\partial r_{n_{(i)}}^{(p)}}, \text{ for } i = 1, 2, \cdots, I, \tag{17}$$

where $r_{n_{(i)}}^{(p)}$ is the estimate of $r_{n_{(i)}}$ after the p^{th} iteration (with $r_{n_{(i)}}^{(0)} = r_{n_{(i)}}^{(k)}$), δ is the step size of the gradient descent, and $\frac{\partial\mathcal{H}}{\partial r_{n_{(i)}}}$ is the partial derivative of the cost function $\mathcal{H}$ with respect to $r_{n_{(i)}}$, which is given as follows

$$\frac{\partial\mathcal{H}(r_{n_{(i)}}^{(p)})}{\partial r_{n_{(i)}}^{(p)}} = a_{n_{(i)}}^{(k+1)}\left(\mathbf{t}\odot\exp\left(-r_{n_{(i)}}^{(p)}\mathbf{t}\right)\right)^T \times\left(a_{n_{(i)}}^{(k+1)}\exp\left(-r_{n_{(i)}}^{(p)}\mathbf{t}\right) - \mathbf{s}_n + c_n^{(k)}\right) + \mu(r_{n_{(i)}}^{(p)} - z_{n_{(i)}}^{(k)} - g_{n_{(i)}}^{(k)}), \text{ for } i = 1, 2, \cdots, I, \tag{18}$$

where $\odot$ is the Hadamard (term-wise) product. Thus the update of $r_{n_{(i)}}^{(k+1)}$ is given by the final solution to the gradient descent algorithm $r_{n_{(i)}}^*$, e.g.,

$$r_{n_{(i)}}^{(k+1)} \leftarrow r_{n_{(i)}}^*, \text{ for } i = 1, 2, \cdots, I. \tag{19}$$

3.3. Solving for $\mathbf{c}$

It can be seen from Eq. (12) that solving for the variable $\mathbf{c}$ reduces to solving the following minimization problem

$$\underset{\mathbf{c}}{\text{minimize}} \quad \sum_{n=1}^{N} \frac{1}{2}\|\mathbf{s}_n - \sum_{i=1}^{I} a_{n_{(i)}} \exp\left(-r_{n_{(i)}}\mathbf{t}\right) - c_n\|_2^2 + \gamma\|\mathbf{c}\|_2^2, \tag{20}$$

whose solution is given by

$$c_n^{(k+1)} \leftarrow \tilde{\gamma}\sum_{m=1}^{M}\left(s_{n_m} - \sum_{i=1}^{I} a_{n_{(i)}}^{(k+1)}\exp\left(-r_{n_{(i)}}^{(k+1)}t_m\right)\right), \tag{21}$$

where $\tilde{\gamma} = 1/(2\gamma + M)$.

3.4. Solving for $\mathbf{y}$

In order to estimate $\mathbf{y}_{(1)}, \cdots, \mathbf{y}_{(I)}$, the optimization problem to solve is

$$\underset{\mathbf{y}_{(1)},\cdots,\mathbf{y}_{(I)}}{\text{minimize}} \quad \sum_{i=1}^{I} \alpha_{(i)} \|\mathbf{y}_{(i)}\|_{\text{TV}} + \sum_{i=1}^{I} \frac{\mu}{2} \|\mathbf{y}_{(i)} - \mathbf{a}_{(i)} - \mathbf{h}_{(i)}\|_2^2, \tag{22}$$

whose solution can be given by Chambolle's algorithm [14], e.g.,

$$\mathbf{y}_{(i)}^{(k+1)} \leftarrow \text{Chambolle}\left(\mathbf{a}_{(i)}^{(k+1)} - \mathbf{h}_{(i)}^{(k)}, \frac{\alpha_{(i)}}{\mu}\right), \text{ for } i = 1, 2, \cdots, I. \tag{23}$$

3.5. Solving for $\mathbf{z}$

In a similar fashion to solving for $\mathbf{y}$, the minimization problem to solve for $\mathbf{z}_{(1)}, \cdots, \mathbf{z}_{(I)}$ is given by

$$\underset{\mathbf{z}_{(1)},\cdots,\mathbf{z}_{(I)}}{\text{minimize}} \quad \sum_{i=1}^{I} \beta_{(i)} \|\mathbf{z}_{(i)}\|_{\text{TV}} + \sum_{i=1}^{I} \frac{\mu}{2} \|\mathbf{z}_{(i)} - \mathbf{r}_{(i)} - \mathbf{g}_{(i)}\|_2^2, \tag{24}$$

whose solution can be given by Chambolle's algorithm [14], e.g.,

$$\mathbf{z}_{(i)}^{(k+1)} \leftarrow \text{Chambolle}\left(\mathbf{r}_{(i)}^{(k+1)} - \mathbf{g}_{(i)}^{(k)}, \frac{\beta_{(i)}}{\mu}\right), \text{ for } i = 1, 2, \cdots, I. \tag{25}$$

Finally, the parameter $\mu > 0$ is updated within the algorithm to keep the primal and dual residual norms within a factor of $\rho = 10$ of one another [12]. The stopping criterion we use is [2,19]

$$\sum_{i=1}^{I} \|\mathbf{y}_{(i)}^{(k)} - \mathbf{a}_{(i)}^{(k)}\|_2 + \|\mathbf{z}_{(i)}^{(k)} - \mathbf{r}_{(i)}^{(k)}\|_2 + \mu\left(\|\mathbf{h}_{(i)}^{(k)} - \mathbf{h}_{(i)}^{(k+\rho)}\|_2 + \|\mathbf{g}_{(i)}^{(k)} - \mathbf{g}_{(i)}^{(k+\rho)}\|_2\right) \leq \epsilon, \tag{26}$$

which is the sum of the primal and dual residuals, where $\epsilon = \sqrt{N} \times 10^{-5}$. Given the detailed updates of the variables mentioned above, several models can be extracted as we will see in the next section.

4. Estimation algorithms

Following the step updates presented in the previous section, the final version of Algorithm 1 is presented in Algorithm 2. Several versions can be derived from this general model, depending on the application. In this section, we extract three models that are widely common in the literature for iron overload quantification using MRI, that are the single exponential (SEXP), the bi-exponential (BiEXP) and the exponential plus constant (CEXP).

4.1. The single exponential (SEXP) model

By setting the offset $\mathbf{c}$ to $\mathbf{c} = \mathbf{0}$, and number of exponential components I to $I = 1$, in the updates of $\mathbf{a}$, $\mathbf{r}$, $\mathbf{y}$, and $\mathbf{z}$ in Equations (14), (19), (23), and (25), respectively, we can obtain Algorithm 3 for the SEXP model.

4.2. The bi-exponential (BiEXP) model

For the BiEXP model, we follow that proposed in [23,26,25,24,42], which can be written as

Algorithm 2 Iron overload estimation using ADMM.

1: set $k = 0$, choose $\mathbf{a}^{(0)}, \mathbf{r}^{(0)}, \mathbf{c}^{(0)}\mathbf{y}^{(0)}, \mathbf{z}^{(0)}, \mathbf{h}^{(0)}, \mathbf{g}^{(0)}$, and $\mu > 0$
2: **repeat** $(k \leftarrow k + 1)$
3: **For** $i = 1 : I$;
4: Update $\mathbf{a}_{(i)}^{(k+1)}$ using Eq. (14),
5: Update $\mathbf{r}_{(i)}^{(k+1)}$ using Eq. (19),
6: Update $\mathbf{y}_{(i)}^{(k+1)}$ using Eq. (23),
7: Update $\mathbf{z}_{(i)}^{(k+1)}$ using Eq. (25),
8: **End**
9: Update $\mathbf{c}^{(k+1)}$ using Eq. (21),
10: **For** $i = 1 : I$;
11: **Update** $\mathbf{h}_{(i)} : \mathbf{h}_{(i)}^{(k+1)} \leftarrow \mathbf{h}_{(i)}^{(k)} - \left(\mathbf{y}_{(i)}^{(k+1)} - \mathbf{a}_{(i)}^{(k+1)}\right)$,
12: **Update** $\mathbf{g}_{(i)} : \mathbf{g}_{(i)}^{(k+1)} \leftarrow \mathbf{g}_{(i)}^{(k)} - \left(\mathbf{z}_{(i)}^{(k+1)} - \mathbf{r}_{(i)}^{(k+1)}\right)$,
13: **End**
14: **until** some stopping criterion is satisfied.

Algorithm 3 Iron overload estimation using **SEXP Model**.

1: **Set** $k = 0$, **Choose** $\mathbf{a}^{(0)}, \mathbf{r}^{(0)}\mathbf{y}^{(0)}, \mathbf{z}^{(0)}, \mathbf{h}^{(0)}, \mathbf{g}^{(0)}, \delta, \mu > 0$
2: **Define** $\mathbf{u}_n^{(l)} = \exp\left(-r_n^{(l)}\mathbf{t}\right)$, $\tilde{\mathbf{u}}_n^{(l)} = \mathbf{u}_n^{(l)^T}\mathbf{u}_n^{(l)}$
3: **Repeat** $(k \leftarrow k + 1)$
4: **For** $n = 1 : N$
5: $a_n^{(k+1)} = \left(\tilde{\mathbf{u}}_n^{(k)} + \mu\right)^{-1}\left(\mathbf{u}_n^{(k)^T}\mathbf{s}_n + \mu\tilde{y_n}^{(k)}\right)$,
with $\tilde{y_n}^{(k)} = y_n^{(k)} + h_n^{(k)}$
6: **Gradient descent algorithm**
Set $p = 0$, and $r_n^{(0)} = r_n^{(k)}$
Repeat $(p \leftarrow p + 1)$
$r_n^{(p+1)} = r_n^{(p)} - \delta\mathcal{H}$
$\mathcal{H} = a_n^{(k+1)}\left(\mathbf{t} \odot \mathbf{u}_n^{(p)}\right)^T\left(a_n^{(k+1)}\mathbf{u}_n^{(p)} - \mathbf{s}_n\right)$
$+\mu(r_n^{(p)} - z_n^{(k)} - h_n^{(k)})$,
until some stopping criterion is satisfied.
$r_n^{(k+1)} = r_n^*$,
7: **End**
8: $\mathbf{y}^{(k+1)} = \text{Chambolle}(\mathbf{a}^{(k+1)} - \mathbf{h}^{(k)}, \frac{\alpha}{\mu})$ which can be computed using [14]
9: $\mathbf{z}^{(k+1)} = \text{Chambolle}(\mathbf{r}^{(k+1)} - \mathbf{g}^{(k)}, \frac{\beta}{\mu})$ which can be computed using [14]
10: $\mathbf{h}^{(k+1)} = \mathbf{h}^{(k)} - \left(\mathbf{y}^{(k+1)} - \mathbf{a}^{(k+1)}\right)$
11: $\mathbf{g}^{(k+1)} = \mathbf{g}^{(k)} - \left(\mathbf{z}^{(k+1)} - \mathbf{r}^{(k+1)}\right)$
12: **until** some stopping criterion is satisfied.

$$\mathbf{S} = \sum_{n=1}^{N=K\times L} 0.9a_n \exp\left(-r_n\mathbf{t}\right) + 0.1a_n \exp\left(-\mathbf{t}/200\right), \tag{27}$$

where, as in comparison with the general model in Eq. (4), the number of exponential components $I = 2$, the offset $\mathbf{c} = \mathbf{0}$, the initial intensity $\mathbf{a}_{(1)}$ and the inverse time constant $\mathbf{r}_{(1)}$ of the first exponential component are given by $\mathbf{a}_{(1)} = 0.9\mathbf{a}$ and $\mathbf{r}_{(1)} = \mathbf{r}$ respectively, and that of the second exponential component are given by $\mathbf{a}_{(2)} = 0.1\mathbf{a}$ and $\mathbf{r}_{(2)} = \{1/200\}^N$, respectively. Thus, in this case, we aim at estimating both $\mathbf{a}$ and $\mathbf{r}$.

By substituting by the above parameters in the updates of $\mathbf{a}$, $\mathbf{r}$, $\mathbf{y}$, and $\mathbf{z}$ in Equations (14), (19), (23), and (25), respectively, we obtain Algorithm 4 for the BiEXP model.

4.3. The exponential plus constant (CEXP) model

By setting the number of exponential components I to $I = 1$, in the updates of $\mathbf{a}$, $\mathbf{r}$, $\mathbf{c}$, $\mathbf{y}$, and $\mathbf{z}$ in Equations (14), (19), (21), (23), and (25), respectively, we obtain Algorithm 5 for the CEXP-model.

5. Simulations using synthetic datasets

In order to assess the performance of the proposed approaches for T2* estimation using T2*-weighted magnetic resonance images, we created simulated datasets by following each of the three models in Equations (5), (7), and (6). A sequence of twelve time-frames of 32×32 each, was created to simulate signal relaxation for image acquisition at different echo times, ranging from 1 to

Algorithm 4 Iron overload estimation using **BiEXP Model**.

Set $k=0$, **Choose** $\mathbf{a}^{(0)}, \mathbf{r}^{(0)} \mathbf{y}^{(0)}, \mathbf{z}^{(0)}, \mathbf{h}^{(0)}, \mathbf{g}^{(0)}, \delta,\ \mu > 0$
Define $\mathbf{u}_n^{(l)} = \exp\left(-r_n^{(l)}\mathbf{t}\right)$, $\tilde{\mathbf{u}}_n^{(l)} = \mathbf{u}_n^{(l)^T}\mathbf{u}_n^{(l)}$,
$\mathbf{w} = \exp\left(-\mathbf{t}/200\right)$, $\tilde{\mathbf{w}} = \mathbf{w}^T\mathbf{w}$
Repeat $(k \leftarrow k+1)$
For $n = 1 : N$
$a_n^{(k+1)} = \left(0.81\tilde{\mathbf{u}}_n^{(k)} + 0.01\tilde{\mathbf{w}} + 0.18\mathbf{w}^T\mathbf{u}_n^{(k)} + \mu\right)^{-1}$
$\left(\mathbf{q}_n^T\mathbf{s}_n + \mu\tilde{y}_n^{(k)}\right)$,
with $\tilde{y}_n^{(k)} = y_n^{(k)} + h_n^{(k)}$ and $\mathbf{q}_n = 0.9\mathbf{u}_n + 0.1\mathbf{w}$
Gradient descent algorithm
Set $p=0$, and $r_n^{(0)} = r_n^{(k)}$
Repeat $(p \leftarrow p+1)$
$r_n^{(p+1)} = r_n^{(p)} - \delta\mathcal{H}$
$\mathcal{H} = 0.9a_n^{(k+1)}\left(\mathbf{t}\odot\mathbf{u}_n^{(p)}\right)^T\left(a_n^{(k+1)}\mathbf{q}_n^{(p)} - \mathbf{s}_n\right)$
$+\mu(r_n^{(p)} - z_n^{(k)} - h_n{}^{(k)})$,
until some stopping criterion is satisfied.
$r_n^{(k+1)} = r_n^*$,
End
$\mathbf{y}^{(k+1)} = \text{Chambolle}(\mathbf{a}^{(k+1)} - \mathbf{h}^{(k)}, \frac{\alpha}{\mu})$ which can be computed using [14]
$\mathbf{z}^{(k+1)} = \text{Chambolle}(\mathbf{r}^{(k+1)} - \mathbf{g}^{(k)}, \frac{\beta}{\mu})$ which can be computed using [14]
$\mathbf{h}^{(k+1)} = \mathbf{h}^{(k)} - \left(\mathbf{y}^{(k+1)} - \mathbf{a}^{(k+1)}\right)$
$\mathbf{g}^{(k+1)} = \mathbf{g}^{(k)} - \left(\mathbf{z}^{(k+1)} - \mathbf{r}^{(k+1)}\right)$
until some stopping criterion is satisfied.

Algorithm 5 Iron overload estimation using **CEXP Model**.

Set $k=0$, **Choose** $\mathbf{a}^{(0)}, \mathbf{r}^{(0)}, \mathbf{c}^{(0)}, \mathbf{y}^{(0)}, \mathbf{z}^{(0)}, \mathbf{h}^{(0)}, \mathbf{g}^{(0)}, \delta,\ \mu > 0$
Define $\mathbf{u}_n^{(l)} = \exp\left(-r_n^{(l)}\mathbf{t}\right)$, $\tilde{\mathbf{u}}_n^{(l)} = \mathbf{u}_n^{(l)^T}\mathbf{u}_n^{(l)}$
Repeat $(k \leftarrow k+1)$
For $n = 1 : N$
$a_n^{(k+1)} = \left(\tilde{\mathbf{u}}_n^{(k)} + \mu\right)^{-1}\left(\mathbf{u}_n^{(k)^T}\tilde{\mathbf{s}}_n^{(k)} + \mu\tilde{y}_n^{(k)}\right)$,
with $\tilde{y}_n^{(k)} = y_n^{(k)} + h_n^{(k)}$, and $\tilde{\mathbf{s}}_n^{(k)} = \mathbf{s}_n - c_n^{(k)}$
Gradient descent algorithm
Set $p=0$, and $r_n^{(0)} = r_n^{(k)}$
Repeat $(p \leftarrow p+1)$
$r_n^{(p+1)} = r_n^{(p)} - \delta\mathcal{H}$
$\mathcal{H} = a_n^{(k+1)}\left(\mathbf{t}\odot\mathbf{u}_n^{(p)}\right)^T\left(a_n^{(k+1)}\mathbf{u}_n^{(p)} - \mathbf{s}_n + c_n\right)$
$+\mu(r_n^{(p)} - z_n^{(k)} - h_n^{(k)})$,
until some stopping criterion is satisfied.
$r_n^{(k+1)} = r_n^*$,
$c_n^{(k+1)} = \frac{1}{2\gamma+M}\sum_{m=1}^{M}\left(s_{n_m} - a_n^{(k+1)}\exp\left(-r_n^{(k+1)}t_m\right)\right)$
End
$\mathbf{y}^{(k+1)} = \text{Chambolle}(\mathbf{a}^{(k+1)} - \mathbf{h}^{(k)}, \frac{\alpha}{\mu})$ which can be computed using [14]
$\mathbf{z}^{(k+1)} = \text{Chambolle}(\mathbf{r}^{(k+1)} - \mathbf{g}^{(k)}, \frac{\beta}{\mu})$ which can be computed using [14]
$\mathbf{h}^{(k+1)} = \mathbf{h}^{(k)} - \left(\mathbf{y}^{(k+1)} - \mathbf{a}^{(k+1)}\right)$
$\mathbf{g}^{(k+1)} = \mathbf{g}^{(k)} - \left(\mathbf{z}^{(k+1)} - \mathbf{r}^{(k+1)}\right)$
until some stopping criterion is satisfied.

16 ms in equal increments, that is $\mathbf{t} \in \mathbb{R}^{12}$. Different model parameters are tested and the results of the three models are reported accordingly. Precisely, different T2* values, belonging to T2*= {5, 10, 15, 20} ms, and different initial intensity values belonging to $a = \{155, 255, 355, 455\}$ are tested. Moreover, in order to test the robustness of the proposed approaches, different noise variances of $\sigma^2 = \{0, 2, 4, 6, 8, 10\}$ are tested. The performance metric adopted in this work to measure the estimation quality of estimated parameters $\hat{\mathbf{x}} = \{\hat{\mathbf{r}}, \hat{\mathbf{a}}\}$ of the three fitting models (SEXP, BiEXP, and CEXP) is root mean square errors (RMSE), calculated between the actual and predicted values, as $\text{RMSE}(\mathbf{x}, \hat{\mathbf{x}}) = \sqrt{\sum_{n=1}^{N}\left(\mathbf{x}(n) - \hat{\mathbf{x}}(n)\right)^2/N}$, where $\mathbf{x}$ and $\hat{\mathbf{x}}$ are vectors of the reference and estimated parameters, respectively.

Different experiments are considered to assess the performance of the proposed approaches. First, we consider simulated images of different T2* values of T2*= {5, 10, 15, 20}, at fixed initial intensity value of $\mathbf{a}_0 = 255$. Second, we consider experiments of simulated images at fixed T2* value of T2*= 20, at different initial intensity values of $\mathbf{a} = \{155, 255, 355, 455\}$. The offset used in the CEXP model is fixed at $\mathbf{c} = 10$. In each experiment, we report RMSE between actual $\mathbf{a}$ (resp. actual T2*) and estimated $\hat{\mathbf{a}}$ (resp. estimated $\hat{\text{T2}}^* = 1/\hat{r}$), that we call $\text{RMSE}_{\mathbf{a}}$ (resp. $\text{RMSE}_{\text{T2}^*}$).

For different T2* at fixed initial intensity value of $\mathbf{a}_0 = 255$, Fig. 2 shows plots of $\text{RMSE}_{\mathbf{a}}$ and $\text{RMSE}_{\text{T2}^*}$ versus different T2* values for the three models, at different noise variances ranging from the free noise case $\sigma^2 = 0$ to the severe noise case of $\sigma^2 = 10$. Similar behaviour is observed for other $\mathbf{a}_0$ values and hence the results are not reported here. As of the noise variance effect, we can observe that, for the SEXP and BiEXP models, as noise variance increases, $\text{RMSE}_{\text{T2}^*}$ and $\text{RMSE}_{\mathbf{a}}$ increase. However, for the CEXP case, this effect is preserved for low T2* values (i.e. T2* = {5, 10}), whereas when T2* increases, $\text{RMSE}_{\text{T2}^*}$ and $\text{RMSE}_{\mathbf{a}}$ become constant. This is due to the identifiability problem when estimating the parameters $\mathbf{a}$ and $\mathbf{c}$ in Eq. (2), as when T2* increases, the decaying curve becomes more linear, making it difficult to the algorithm to distinguish the estimation of both $\mathbf{c}$ and $\mathbf{a}$. On the other hand, for the different T2* values effect, for the three models, we can observe that when T2* increases, $\text{RMSE}_{\text{T2}^*}$ increases, whereas $\text{RMSE}_{\mathbf{a}}$ decreases. Considering the mean or median values of estimated T2* and $\mathbf{a}$ reduce $\text{RMSE}_{\text{T2}^*}$ and $\text{RMSE}_{\mathbf{a}}$ significantly, as estimated values become very close to actual ones, as shown in Fig. 3.

On the other hand, for different initial intensity values $\mathbf{a}$ at fixed T2* = 20 (similar behaviour is observed for other T2* values and hence the results are not reported here), Fig. 4 shows plots of $\text{RMSE}_{\mathbf{a}}$ and $\text{RMSE}_{\text{T2}^*}$ versus different T2* values for the three approaches, at different noise variances ranging from the free noise case $\sigma^2 = 0$ to the severe noise case $\sigma^2 = 10$. As of noise variance effect, we can observe that, for the SEXP and BiEXP models, as noise variance increases, $\text{RMSE}_{\text{T2}^*}$ and $\text{RMSE}_{\mathbf{a}}$ increase. However, for the CEXP case, due to the identifiability problem mentioned earlier, when estimating the parameters $\mathbf{a}$ and $\mathbf{c}$, both $\text{RMSE}_{\text{T2}^*}$ and RMSE_a become higher than those of the SEXP and BiEXP cases for the tested noise variances. As similar to the experiments of fixed $\mathbf{a}$ mentioned earlier, considering the mean value of estimated T2* and $\mathbf{a}$ reduce both $\text{RMSE}_{\text{T2}^*}$ and RMSE_a significantly, as estimated values become very close to actual ones, except for the CEXP model, as shown in Fig. 5.

For completeness, we show visual examples of experiments of estimated $\mathbf{a}$ and T2*. Fig. 6 shows in (a) an image of 64×64 of different initial intensity values of $\mathbf{a} = [155, 255, 355, 455]$ and in (b) the corresponding T2* values of T2*= [5, 10, 15, 20]. Consequently, Fig. 7 shows the resulting first frame when applying the SEXP, BiEXP and CEXP models in Equations (5), (6), and (7) respectively. The offset $\mathbf{c}$ in the CEXP model is set to $\mathbf{c} = 25$, and two different noise variances are presented; the noise free case $\sigma^2 = 0$, and a severe noise case of $\sigma^2 = 10$. The SEXP, BiEXP and CEXP algorithms in 3, 4 and 5 are then run to estimate $\mathbf{a}$ and T2*. Figs. 8 and 9 show estimated $\mathbf{a}$ in the free and severe noise cases. We can observe that, in the SEXP and BiEXP cases, the restored images are similar to those of the ground truth, whereas for the CEXP case, it is slightly different as because of the identifiability problem when estimating both $\mathbf{a}$ and $\mathbf{c}$, as mentioned earlier. Moreover, for the noisy case, when considering the means of estimated values, the resulting estimates become closer to ground truth values. On the other hand, Figs. 10 and 11 show the corresponding estimated T2* images. As similar to $\mathbf{a}$, the SEXP and BiEXP models provide very similar results to the actual T2* images, whereas slightly different for the CEXP, for the similar identifiability problem mentioned earlier. Moreover, considering the mean of estimated T2* of each block provides closer results to ground truth in the noisy case.

The proposed approaches are compared with the Levenberg-Marquardt (LM) fitting algorithm, which is widely used in the

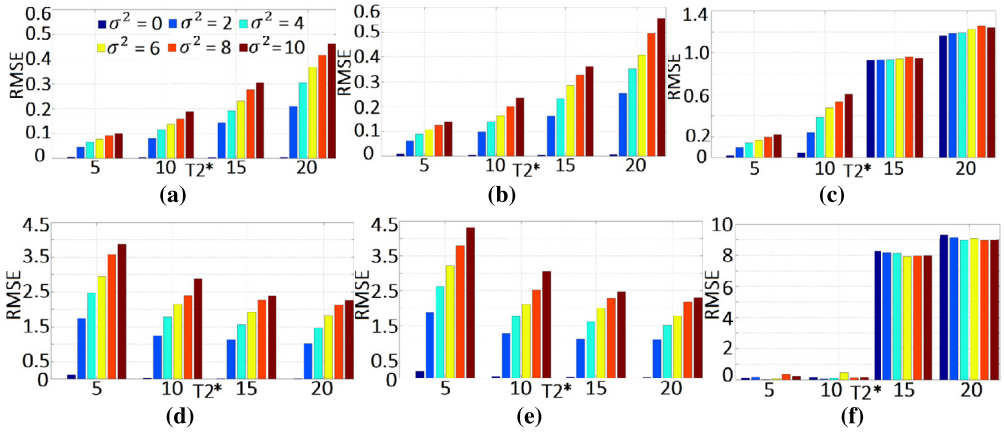

Fig. 2. Plots of RMSE between actual T2* and estimated ones ($\text{RMSE}_{\text{T2}^*}$) in Row 1; and RMSE between actual initial intensity value $\mathbf{a}_0$ and estimated ones ($\text{RMSE}_{\mathbf{a}}$) in Row 2, at fixed initial intensity value $\mathbf{a}_0 = 255$ for different T2* values and different noise variances (σ^2). Column 1: SEXP model; Column 2: BiEXP model, and Column 3: CEXP model.

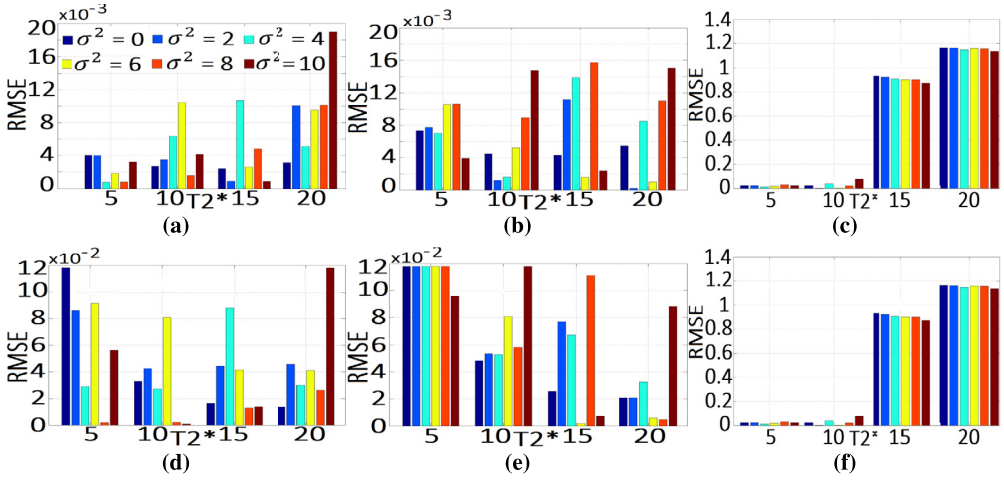

Fig. 3. Plots of RMSE between actual T2* and means of estimated ones ($\text{RMSE}_{\text{T2}^*}$) in Row 1; and RMSE between actual initial intensity value $\mathbf{a}_0$ and means of estimated ones ($\text{RMSE}_{\mathbf{a}}$) in Row 2, at fixed initial intensity value $\mathbf{a}_0 = 255$ for different T2* values and different noise variances (σ^2). Column 1: SEXP model; Column 2: BiEXP model, and Column 3: CEXP model.

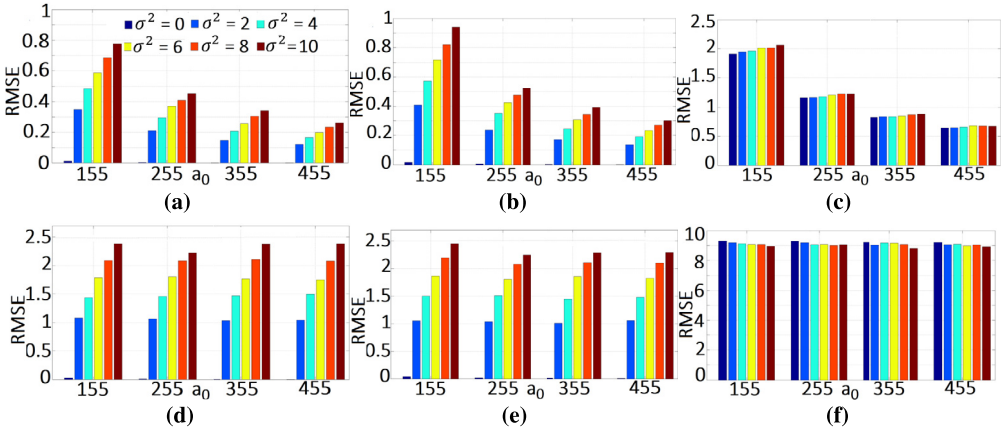

Fig. 4. Plots of RMSE between actual T2* and estimated ones ($\text{RMSE}_{\text{T2}^*}$) in Row 1, and RMSE between actual initial intensity value $\mathbf{a}_0$ and estimated ones ($\text{RMSE}_{\mathbf{a}}$) in Row 2, at fixed $\text{T2}^* = 20$, for different initial intensity values $\mathbf{a}$ and different noise variances (σ^2). Column 1: SEXP model; Column 2: BiEXP model, and Column 3: CEXP model.

literature for T2* estimation in MRI problems [27,26,37], and a linear fitting (LF) algorithm [11]. The LM, which is a damped least square fitting algorithm, is considered as a fitting method for the three models SEXP, BiEXP and CEXP in Equations (5), (6) and (7) respectively, whereas the LF algorithm is considered for the SEXP model. The built-in matlab function *lsqcurvefit* is used for the LM algorithm. Table 1 provides a comparison between T2* estimation using the proposed approaches and the LM and LF algorithms, for different T2*, $\mathbf{a}$, and σ^2. We can observe that the proposed approaches provide better estimation performance in most of tested experiments. This is probably because the nature of the proposed approaches in promoting spatial correlation between neighbouring

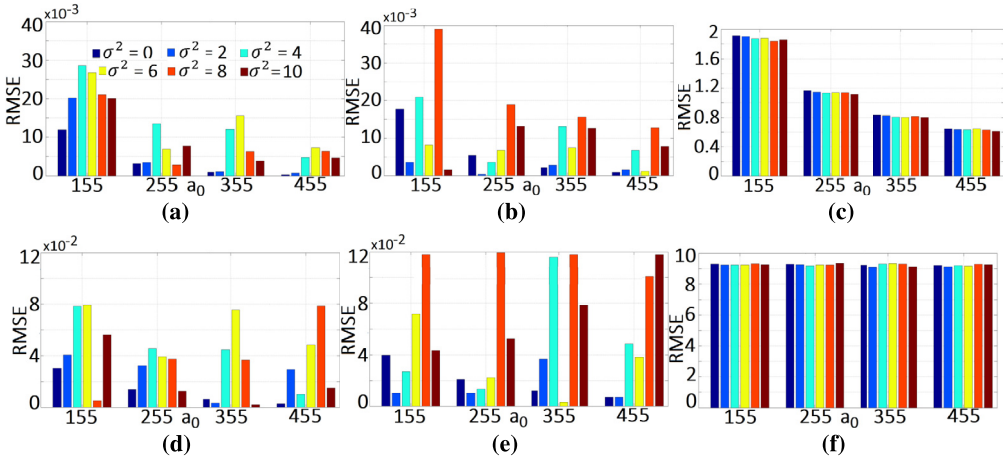

Fig. 5. Plots of RMSE between actual T2* and mean of estimated ones (RMSE_{T2^*}) in Row 1, and RMSE between actual initial intensity value $\mathbf{a}_0$ and mean of estimated ones ($\text{RMSE}_{\mathbf{a}}$) in Row 2, at fixed T2* = 20, for different initial intensity values **a** and different noise variances (σ^2). Column 1: SEXP model; Column 2: BiEXP model, and Column 3: CEXP model.

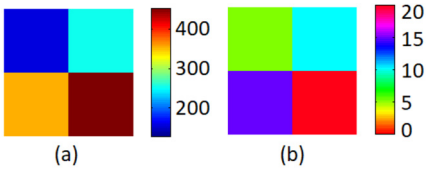

Fig. 6. (a) Image of 64 × 64 of different initial intensity values of $\mathbf{a} = [155, 255, 355, 455]$ and (b) the corresponding T2* values T2* = [5, 10, 15, 20].

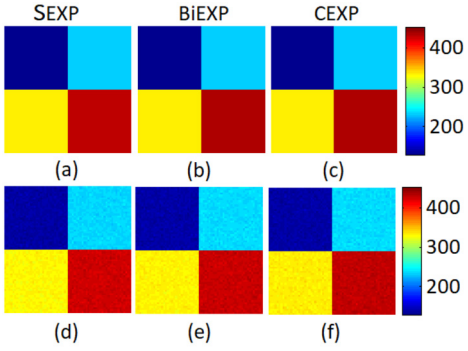

Fig. 7. The resulting first frame when applying the models in Equations (5) for the SEXP model (a) and (d); (6) for the BiEXP model (b) and (e); and (7) for the CEXP model when setting $c = 25$ (c) and (f). Row 1: in the noise free case $\sigma = 0$, and Row 2: the severe noise case $\sigma^2 = 10$.

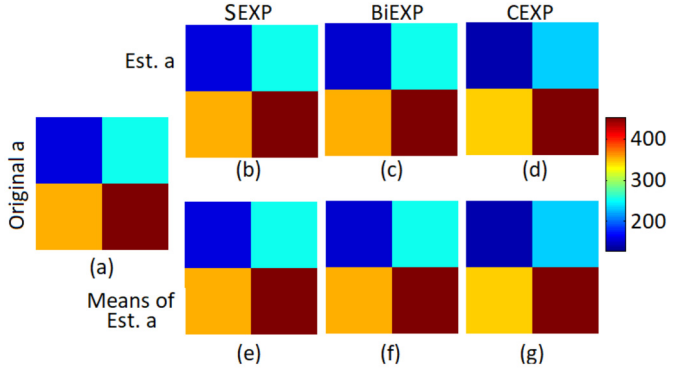

Fig. 8. Initial intensity value (**a**) estimation using the proposed approaches in the noise free case. (a) Original **a**, and results of estimation of **a**, in the noise free case, using the (b) SEXP, (c) BiEXP and (d) CEXP models. (e), (f) and (g) show the corresponding estimates when considering the mean of estimated **a** in each case.

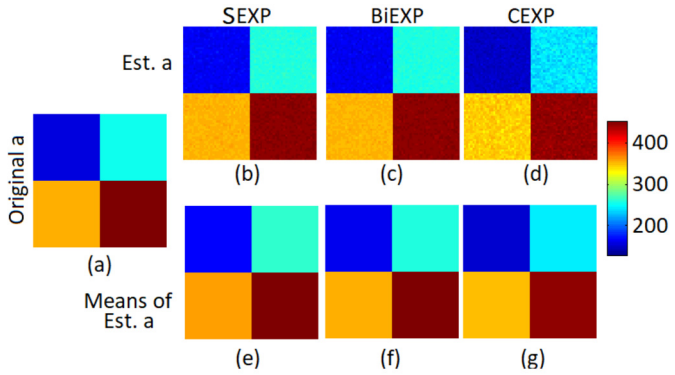

Fig. 9. Initial intensity value (**a**) estimation using the proposed approaches for $\sigma^2 = 10$. (a) Original **a**, and results of estimation of **a**, in the noise free case, using the (b) SEXP, (c) BiEXP and (d) CEXP models. (e), (f) and (g) show the corresponding estimates when considering the mean of estimated **a** in each case.

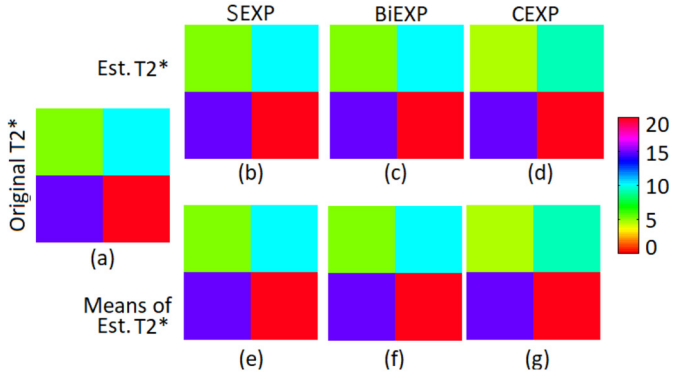

Fig. 10. Relaxation time (T2*) estimation using the proposed approaches in the noise free case. (a) Original T2*, and results of estimation of T2*, in the noise free case, using the (b) SEXP, (c) BiEXP and (d) CEXP models. (e), (f) and (g) show the corresponding estimates when considering the mean of estimated T2* in each case.

voxels using TV regularization functions, compared to the LM algorithm which provides a least-squares estimation.

As of computation time, Table 2 provides the average computation time of ten runs of each of the three proposed approaches, and existing methods described above. The algorithms are implemented in MATLAB and the experiments are carried out on a laptop with a 2.8 GHz processor CPU, with 16 GB of RAM, under Microsoft Windows 10. Experiments of different T2* and initial

Table 1
Comparison between the proposed approaches and Levenberg-Marquardt (LM) and linear fitting (LF) algorithms, using RMSE between actual and estimated T2*. Best results are highlighted in bold.

	a_0	155				455			
	σ^2	5		10		5		10	
Model	T2*	5	20	5	20	5	20	5	20
SEXP	Pr	**0.01**	**0.01**	**0.02**	**0.02**	**0.001**	**0.001**	**0.004**	**0.005**
	LM	**0.01**	0.09	0.03	0.2	0.002	0.9	0.006	1.1
	LF	0.09	**0.01**	0.25	0.03	0.01	0.001	0.01	0.01
BiEXP	Pr	**0.01**	**0.02**	**0.01**	**0.01**	**0.01**	**0.01**	**0.01**	**0.01**
	LM	**0.01**	0.08	**0.01**	0.16	**0.01**	0.8	0.02	0.9
CEXP	Pr	0.06	1.8	0.3	1.8	**0.01**	**0.01**	**0.1**	**0.6**
	LM	**0.03**	**0.9**	**0.04**	**1.4**	0.5	8.1	0.6	9.6

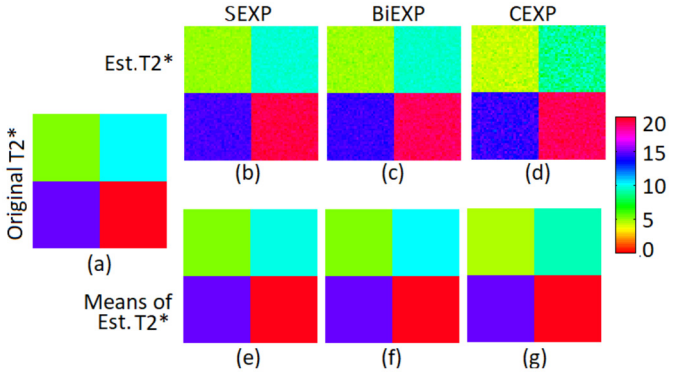

Fig. 11. Relaxation time (T2*) estimation using the proposed approaches for $\sigma^2 = 10$. (a) Original T2*, and results of estimation of T2*, in the noise free case, using the (b) SEXP, (c) BiEXP and (d) CEXP models. (e), (f) and (g) show the corresponding estimates when considering the mean of estimated T2* in each case.

Table 2
Approximate computation time in seconds for the proposed approaches and existing methods.

	Proposed			Levenberg-Marquardt			Linear Fitting
Model	SEXP	BiEXP	CEXP	SEXP	BiEXP	CEXP	SEXP
Time	4	7	8	4	6	12	1

intensity values $\mathbf{a}_0$ are run and the mean computation time is reported. It is clear that the LF algorithm provides the least computation cost. However, the proposed approaches provide competitive computation time with respect to the LM algorithm. Moreover, the SEXP algorithm always provides the least computation cost, then BiEXP, and finally CEXP.

6. Simulations using patient datasets

In-vivo scans of the abdomen of nine human subjects with sickle cell disease (five males, four females; age: 38 ± 12 years) were imaged on a 3.0-Tesla Siemens Skyra MRI scanner (Siemens Healthcare, Erlangen, Germany) using a body surface coil and a 8-echo gradient echo (GRE) sequence with TEs ranging from 1 to 16.4 ms in equal increments. The imaging parameters were as follows: repetition time (TR) = 5200 msec, matrix 192×256; bandwidth = 1776 Hz/pixel, flip angle = 20°, slice thickness = 10 mm, and field of view that depended on the patient size. A mid-liver axial slice was acquired in a single end-expiration breath-hold. Informed consent in this Institutional Review Board-approved study was given for this study. Fig. 12 shows a sequence of T2* weighted images of the abdomen of a patient included in this study, with the parameters mentioned above. We can observe the decay of signal intensity in the liver as TE increases. Due to the heterogeneous iron concentration in the liver, susceptibility artifacts, and inclusion of vasculature, T2* measurements can be different in different parts of the liver. As observed in the results using synthetic data, that computing the average of T2* in a defined region results in better estimation performance, in this work, we consider T2* estimation in a region of interest (ROI) in the liver as in [27,26,24,23,25]. Fig. 13 shows the location of ROI used to estimate the T2*, as identified by a trained clinician. The location of the selected ROI was not exactly the same for all patients; however, it was selected away from the boundary and vasculature in the region of most homogeneous signal intensity in the right lobe. In this study, reference standard biopsy samples from the patients indicating iron overload content were not acquired, as this was not part of standard-of-care procedures. However, T2* values measured on the MRI scanner console were obtained for the ROIs, and are considered for comparison. Algorithms 3, 4, and 5 are run to estimate T2* for each patient. We investigate averaging (T2*-AVG) values of T2* estimates of the ROI. In all cases, the regularization parameters (α, β, γ) are set to $(\alpha, \beta, \gamma) = (10^{-3}, 10^{-3}, 10^{-3})$. Note that we did not observe noticeable changes in T2* estimates when we slightly changed these hyperparameters.

As mentioned earlier, the proposed approaches are compared against the Levenberg-Marquardt (LM) and linear fitting (LF) algorithms. For the LM and LF algorithms, several post-analysis techniques are applied to obtain final T2* values. In particular, T2*-pixel-wise, where exponential fitting is applied to each pixel inside the ROI, followed by obtaining the mean (T2*-AVG) of the resulting T2* values, and, averaging signal intensities (Sig-AVG) inside the ROI, followed by exponential fitting of the resulting values at different TEs, to obtain the final T2* measurement.

Table 3 provides T2* measurements of the nine patients using the MRI scanner console, the proposed approaches and the existing methods mentioned above. We can observe that the results of proposed SEXP and CEXP models are quite similar, compared to those of the BiEXP model. On the other hand, we can observe that there is small difference between T2* estimation using T2*-AVG and Sig-AVG using the LM algorithm. In general, the proposed approaches provide the closest measurements to those of the scanner console, compared to the LM and LF algorithms. In particular, in terms of fitting model, the SEXP and the CEXP models provide the closest measurements to those the scanner console compared to those of the BiEXP model. This is probably because the ROIs chosen in this work are vasculature free and hence signal fitting is more accurate using the SEXP and the CEXP models, and that T2* estimation using the scanner console considered SEXP/CEXP models.

7. Limitations

Although the benefits of the proposed approaches in estimating T2* are clear, a few limitations remain. The first is related to the lack of ground truth iron concentration for the patient datasets investigated in this work, as this was not part of standard-of-care

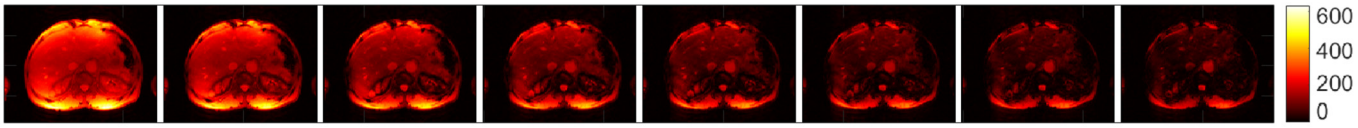

Fig. 12. A sequence of liver images of different time to echo, of a patient with mild iron overload.

Table 3
T2* estimation for patient data using the proposed approaches, and comparison with console and existing methods. Close results to the scanner console are highlighted.

			Patients								
Method	Analysis	Model	1	2	3	4	5	6	7	8	9
MRI Console			**9.1**	**9.1**	**4.3**	**16.2**	**4.2**	**8.9**	**13.6**	**6.1**	**10.7**
Proposed	T2*-AVG	SEXP	9.2	9.4	**4.4**	**16.2**	3.6	**9.0**	**11.7**	**6.2**	**10.8**
		BiEXP	7.2	7.4	3.7	13.6	3.4	7.0	9.5	5.0	8.7
		CEXP	**9.1**	9.4	**4.2**	15.8	3.5	**9.0**	11.4	**6.3**	**10.8**
Levenberg-Marquardt	T2*-AVG	SEXP	9.3	9.7	4.4	15.6	3.6	8.0	9.5	5.6	11.4
		BiEXP	14.0	17.6	3.8	21.0	3.7	13.4	18.3	13.0	20.5
		CEXP	14.2	17.7	3.9	21.0	3.8	13.6	18.4	13.1	20.6
	Sig-AVG	SEXP	9.4	9.9	4.1	15.5	3.7	8.6	11.0	5.8	11.3
		BiEXP	13.6	18.2	3.7	22.6	3.7	12.8	21.3	13.0	20.9
		CEXP	13.9	18.6	3.8	22.7	3.8	13.0	21.3	13.1	20.8
Linear Fitting	T2*-AVG	SEXP	8.2	8.6	6.1	15.2	4.1	7.0	7.7	5.1	9.9
	Sig-AVG	SEXP	8.8	8.9	5.4	15.3	4.4	7.6	9.4	5.4	9.9

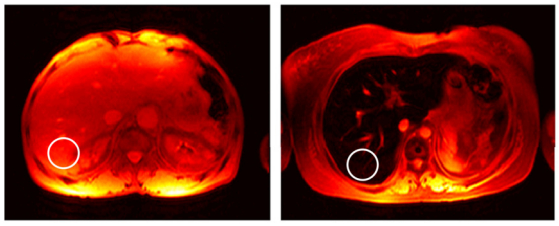

Fig. 13. T2* weighted images for mild (Left) and severe (Right) iron overload patients. The white circles indicate the location and size of the ROI used for analysis.

procedures. Liver biopsy is the current gold standard technique for iron overload quantification. However, due to the technique's invasiveness, pain, and high cost, it limits its widespread use. The second limitation is related to the lack of knowledge about the algorithm and the fitting model (SEXP, BiEXP or CEXP) used for T2* estimation using the MRI scanner console, which is used for comparison in this work. Although T2* estimates are provided for each patient, these measurements cannot be considered as ground truth. We note that in clinical context no ground truth will exist and it is a topic of further work.

8. Conclusion and future work

This paper introduced a general framework for T2* estimation in MRI. The problem was formulated as a minimization problem and suitable regularization functions were assigned to the unknown model parameters. An efficient estimation algorithm using the alternating direction method of multipliers was then used to estimate the unknown model parameters. Three different algorithms were extracted, implying different physical phenomena, including the single exponential (SEXP), the bi-exponential (BiEXP) and the exponential plus constant (CEXP). Other algorithms can still be derived depending on the application. Extensive simulations conducted using synthetic datasets, where ground truth is available, were conducted. The three models provided good estimation performance to the unknown model parameters. It was found that introducing TV regularization in general provides better parameter estimation performance than using a damped least-square method (Levenberg–Marquardt algorithm) and linear fitting. Consequently, the algorithms were validated using a hepatic iron overload quantification problem of patients of different iron overload content. The T2* estimation results of the proposed approaches were found to correlate with those obtained by the MRI scanner console. Moreover, the proposed algorithms outperformed existing methods in the literature for T2* estimation. Future work includes correlating T2* measurements with iron overload concentration, and investigating T2* estimation in other parts in the liver.

CRediT authorship contribution statement

Ahmed Karam Eldaly: Conceptualization, Methodology, Software, Writing – original draft, Writing – review & editing. **Ayman M. Khalifa:** Data curation, Investigation, Writing – review & editing.

Declaration of competing interest

The authors declare that they have no known competing financial interests or personal relationships that could have appeared to influence the work reported in this paper.

Data availability

Data will be made available on request.

References

[1] P.C. Adams, Y. Deugnier, R. Moirand, P. Brissot, The relationship between iron overload, clinical symptoms, and age in 410 patients with genetic hemochromatosis, Hepatology 25 (1997) 162–166.
[2] M.V. Afonso, J.M. Bioucas-Dias, M.A. Figueiredo, An augmented lagrangian approach to the constrained optimization formulation of imaging inverse problems, IEEE Trans. Image Process. 20 (2011) 681–695.
[3] L. Anderson, S. Holden, B. Davis, E. Prescott, C. Charrier, N. Bunce, D. Firmin, B. Wonke, J. Porter, J. Walker, et al., Cardiovascular t2-star (t2*) magnetic resonance for the early diagnosis of myocardial iron overload, Eur. Heart J. 22 (2001) 2171–2179.
[4] L.J. Anderson, B. Wonke, E. Prescott, S. Holden, J.M. Walker, D.J. Pennell, Comparison of effects of oral deferiprone and subcutaneous desferrioxamine on myocardial iron concentrations and ventricular function in beta-thalassaemia, Lancet 360 (2002) 516–520.
[5] E. Angelucci, G.M. Brittenham, C.E. Mclaren, M. Ripalti, D. Baronciani, C. Giardini, M. Galimberti, P. Polchi, G. Lucarelli, Hepatic iron concentration and total body iron stores in thalassemia major, N. Engl. J. Med. 343 (2000) 327–331.

[6] W. Bano, G.F. Piredda, M. Davies, I. Marshall, M. Golbabaee, R. Meuli, T. Kober, J.P. Thiran, T. Hilbert, Model-based super-resolution reconstruction of t2 maps, Magn. Reson. Med. 83 (2020) 906–919.
[7] M.L. Bassett, J.W. Halliday, L.W. Powell, Value of hepatic iron measurements in early hemochromatosis and determination of the critical iron level associated with fibrosis, Hepatology 6 (1986) 24–29.
[8] M. Beaumont, I. Odame, P.S. Babyn, L. Vidarsson, M. Kirby-Allen, H.L.M. Cheng, Accurate liver t measurement of iron overload: a simulations investigation and in vivo study, J. Magn. Reson. Imaging 30 (2009) 313–320.
[9] S. Bondestam, A. Lamminen, V.J. Anttila, T. Ruutu, P. Ruutu, Magnetic resonance imaging of transfusional hepatic iron overload, Br. J. Radiol. 67 (1994) 339–341.
[10] J.M. Bonny, M. Zanca, J.Y. Boire, A. Veyre, T2 maximum likelihood estimation from multiple spin-echo magnitude images, Magn. Reson. Med. 36 (1996) 287–293.
[11] S. Boyd, S.P. Boyd, L. Vandenberghe, Convex Optimization, Cambridge University Press, 2004.
[12] S. Boyd, N. Parikh, E. Chu, B. Peleato, J. Eckstein, Distributed optimization and statistical learning via the alternating direction method of multipliers, Found. Trends Mach. Learn. 3 (2011) 1–122.
[13] A. Carneiro, J. Fernandes, M. Zago, D. Covas, I. Angulo, O. Baffa, An alternating current superconductor susceptometric system to evaluate liver iron overload, Rev. Sci. Instrum. 74 (2003) 3098–3103.
[14] A. Chambolle, An algorithm for total variation minimization and applications, J. Math. Imaging Vis. 20 (2004) 89–97.
[15] E.K. Chong, S.H. Zak, An Introduction to Optimization, John Wiley & Sons, 2004.
[16] A. Christoforidis, V. Perifanis, G. Spanos, E. Vlachaki, M. Economou, I. Tsatra, M. Athanassiou-Metaxa, Mri assessment of liver iron content in thalassamic patients with three different protocols: comparisons and correlations, Eur. J. Haematol. 82 (2009) 388–392.
[17] P.R. Clark, W. Chua-Anusorn, T.G. St Pierre, Bi-exponential proton transverse relaxation rate (r2) image analysis using rf field intensity-weighted spin density projection: potential for r2 measurement of iron-loaded liver, Magn. Reson. Imaging 21 (2003) 519–530.
[18] K.H. Ehlers, A.R. Levin, A.L. Markenson, J.R. Marcus, A.A. Klein, M.W. Hilgartner, M.A. Engle, Longitudinal study of cardiac function in thalassemia major, Ann. N.Y. Acad. Sci. 344 (1980) 397–404.
[19] A.K. Eldaly, Y. Altmann, A. Perperidis, N. Krstajic, T.R. Choudhary, K. Dhaliwal, S. McLaughlin, Deconvolution and restoration of optical endomicroscopy images, IEEE Trans. Comput. Imaging 4 (2018) 194–205, https://doi.org/10.1109/TCI.2018.2811939.
[20] N. Fujita, R. Sugimoto, N. Urawa, et al., Hepatic iron accumulation is associated with disease progression and resistance to interferon/ribavirin combination therapy in chronic hepatitis C, J. Gastroenterol. Hepatol. 22 (2007) 1886–1893.
[21] M. Golbabaee, G. Buonincontri, C.M. Pirkl, M.I. Menzel, B.H. Menze, M. Davies, P.A. Gómez, Compressive mri quantification using convex spatiotemporal priors and deep encoder-decoder networks, Med. Image Anal. 69 (2021) 101945.
[22] T. He, P.D. Gatehouse, G.C. Smith, R.H. Mohiaddin, D.J. Pennell, D.N. Firmin, Myocardial t measurements in iron-overloaded thalassemia: an in vivo study to investigate optimal methods of quantification, Magn. Reson. Med. 60 (2008) 1082–1089.
[23] E.S. Ibrahim, A. Khalifa, A. Eldaly, Influence of the analysis technique on estimating hepatic iron content using mri, J. Magn. Reson. Imaging 44 (2016) 1448–1455.
[24] E.S.H. Ibrahim, A.M. Khalifa, A.K. Eldaly, The influence of the analysis technique on estimating liver iron overload using magnetic resonance imaging t2* quantification, in: 2014 36th Annual International Conference of the IEEE Engineering in Medicine and Biology Society, IEEE, 2014, pp. 4639–4642.
[25] E.S.H. Ibrahim, A.M. Khalifa, A.K. Eldaly, Mri t2* imaging for assessment of liver iron overload: study of different data analysis approaches, Acta Radiol. 57 (2016) 1453–1459.
[26] E.S.H. Ibrahim, A.M. Khalifa, A.K. Eldaly, A.W. Bowman, The effects of the analysis technique on hepatic iron evaluation using t2* mapping with magnetic resonance imaging, in: 2nd Middle East Conference on Biomedical Engineering, 2014, pp. 13–16.
[27] E.S.H. Ibrahim, F.N. Rana, K.R. Johnson, R.D. White, Assessment of cardiac iron deposition in sickle cell disease using 3.0 Tesla cardiovascular magnetic resonance, Hemoglobin 36 (2012) 343–361.
[28] A. Kolnagou, C. Economides, E. Eracleous, G.J. Kontoghiorghes, Low serum ferritin levels are misleading for detecting cardiac iron overload and increase the risk of cardiomyopathy in thalassemia patients. The importance of cardiac iron overload monitoring using mri t2 and t2, Hemoglobin 30 (2006) 219–227.
[29] T.G. Maris, O. Papakonstantinou, V. Chatzimanoli, A. Papadakis, K. Pagonidis, N. Papanikolaou, A. Karantanas, N. Gourtsoyiannis, Myocardial and liver iron status using a fast t quantitative mri (t qmri) technique, Magn. Reson. Med. 57 (2007) 742–753.
[30] J. Nocedal, S. Wright, Numerical Optimization, Springer Science & Business Media, 2006.
[31] O. Papakonstantinou, E. Alexopoulou, N. Economopoulos, O. Benekos, A. Kattamis, S. Kostaridou, V. Ladis, E. Efstathopoulos, A. Gouliamos, N.L. Kelekis, Assessment of iron distribution between liver, spleen, pancreas, bone marrow, and myocardium by means of r2 relaxometry with mri in patients with β-thalassemia major, J. Magn. Reson. Imaging 29 (2009) 853–859.
[32] A. Pepe, M. Lombardi, V. Positano, E. Cracolici, M. Capra, R. Malizia, L. Prossomariti, D. De Marchi, M. Midiri, A. Maggio, Evaluation of the efficacy of oral deferiprone in β-thalassemia major by multislice multiecho t2, Eur. J. Haematol. 76 (2006) 183–192.
[33] A. Pietrangelo, Non-invasive assessment of hepatic iron overload: are we finally there?, J. Hepatol. 42 (2005) 153–154.
[34] V. Positano, B. Salani, A. Pepe, M.F. Santarelli, D. De Marchi, A. Ramazzotti, B. Favilli, et al., Improved t2* assessment in liver iron overload by magnetic resonance imaging, Magn. Reson. Imaging 27 (2009) 188–197.
[35] V. Positano, B. Salani, B. Scattini, M.F. Santarelli, A. Ramazzotti, A. Pepe, M. Lombardi, L. Landini, A robust method for assessment of iron overload in liver by magnetic resonance imaging, in: 2007 29th Annual International Conference of the IEEE Engineering in Medicine and Biology Society, IEEE, 2007, pp. 2895–2898.
[36] L.I. Rudin, S. Osher, E. Fatemi, Nonlinear total variation based noise removal algorithms, Phys. D: Nonlinear Phenom. 60 (1992) 259–268.
[37] J.K. Ryu, J.H. Oh, H.G. Kim, S.J. Rhee, M. Seo, G.H. Jahng, Estimation of t2* relaxation times for the glandular tissue and fat of breast at 3t mri system, J. Korean Soc. Magn. Reson. Med. 18 (2014) 1–6.
[38] E.S. Siegelman, D.G. Mitchell, R. Rubin, H. Hann, K. Kaplan, R. Steiner, V. Rao, S. Schuster, D. Burk Jr, M. Rifkin, Parenchymal versus reticuloendothelial iron overload in the liver: distinction with mr imaging, Radiology 179 (1991) 361–366.
[39] C.B. Sirlin, S.B. Reeder, Magnetic resonance imaging quantification of liver iron, Magn. Res. Imaging Clin. 18 (2010) 359–381.
[40] J. Wood, C. Enriquez, N. Ghugre, M. Tyzka, S. Carson, M. Nelson, T. Coates, Mri r2 and r2* mapping accurately estimates hepatic iron concentration in transfusion-dependent thalassemia and sickle cell disease patients, Blood 106 (2005) 1460–1465.
[41] J.C. Wood, Magnetic resonance imaging measurement of iron overload, Curr. Opin. Hematol. 14 (2007) 183.
[42] J.C. Wood, N. Ghugre, Magnetic resonance imaging assessment of excess iron in thalassemia, sickle cell disease and other iron overload diseases, Hemoglobin 32 (2008) 85–96.

Ahmed Karam Eldaly received a Joint Erasmus Mundus Masters degree in computer vision and robotics from Heriot-Watt University - UK, Université de Bourgone - France, and Universitat de Girona – Spain. Following this, he was awarded the PhD degree in Electrical, Electronic and Computer Engineering from Heriot-Watt University – UK. He is currently a Research Fellow in Computer Science at University College London – UK. His research interests span machine learning, statistical signal and image processing and computational imaging, with applications to medical imaging.

Ayman M. Khalifa obtained his Bachelor, Master, and Ph.D. degrees in biomedical engineering from Cairo University, Egypt in 1997, 2001 and 2007, respectively. He is currently a department chair and full professor of Biomedical Engineering at Helwan University, Egypt, where he has been since 2001. His research interests span medical imaging, image processing, computer vision and healthcare IT.